A Lifting-Line Approach to Estimating Propeller/Wing Interactions

Douglas Hunsaker[*] and Deryl Snyder[†]

Brigham Young University, Provo, Utah, 84602

A combined wing and propeller model is presented as a low-cost approach to first-cut modeling of slipstream effects on a finite wing. The wing aerodynamic model employs a numerical lifting-line method utilizing the 3D vortex lifting law along with known 2D airfoil data to predict the lift distribution across a wing for a prescribed upstream flowfield. The propeller/slipstream model uses a blade element theory combined with momentum conservation equations. This model is expected to be of significant importance in the design of tail-sitter vertical take-off and landing (VTOL) aircraft, where the propeller slipstream is the primary source of air flow past the wings in some flight conditions. The algorithm is presented, and results compared with published experimental data.

Nomenclature

A_i	area of wing section i
$\bar{c}_i$	characteristic chord length for wing section i
c_i	average chord length at wing section i
C_{Di}	section drag coefficient for wing section i
C_{Li}	section lift coefficient for wing section i
$C_{L\alpha i}$	section lift slope for wing section i
C_{Mi}	section moment coefficient for wing section i
$\mathbf{d\ell_i}$	directed differential vortex length vector at control point i
$\mathbf{dF_i}$	section aerodynamic force vector for wing section i
dF_i	magnitude of $\mathbf{dF_i}$
f	system of equations
$\mathbf{F}$	total force on aircraft
$[\mathbf{J}]$	Jacobian matrix
$\mathbf{M}$	total moment on aircraft
N	total number of horseshoe vortices
$\mathbf{R}$	residual vector
$\mathbf{r_i}$	vector from aircraft CG to control point i
$\mathbf{r_{i_1 j}}$	vector from 1st node on section i to control point on section j
$\mathbf{r_{i_2 j}}$	vector from 2nd node on section i to control point on section j
$r_{i_1 j}$	magnitude of $\mathbf{r_{i_1 j}}$
$r_{i_2 j}$	magnitude of $\mathbf{r_{i_2 j}}$
S_i	planform area of wing section i
$\mathbf{u_{ai}}$	chordwise unit vector at control point i
$\mathbf{u_{ni}}$	normal unit vector at control point i
$\mathbf{u_{si}}$	spanwise unit vector at control point i
$\mathbf{u_i}$	unit vector in the direction of the local velocity
$\mathbf{v_{ij}}$	velocity induced at control point j by horseshoe vortex i
$\mathbf{V_i}$	velocity vector at control point i

---

[*]Student Research Assistant, doug.hunsaker@byu.edu, AIAA Student Member
[†]Assistant Professor, Mechanical Engineering Department, deryl.snyder@byu.edu, AIAA Member

V_i	magnitude of $\mathbf{V_i}$
V_{ai}	axial component of the velocity at control point i
V_{ni}	normal component of the velocity at control point i
$\mathbf{V_{rel_i}}$	upstream velocity at control point i
$\mathbf{V_{tot_i}}$	total velocity at control point i
V_{tot_i}	magnitude of $\mathbf{V_{tot_i}}$
α_i	angle of attack at wing section i
α_{L0i}	zero-lift angle of attack for with section i
δ_i	flap deflection for wing section i
$\delta\mathbf{M_i}$	section quarter-chord moment coefficient at wing section i
$\delta\mathbf{M}_{visc_i}$	viscous correction to the moment coefficient for wing section i
ϵ_i	flap efficiency for wing section i
$\boldsymbol{\Gamma}$	vector of vortex strengths
Γ_i	vortex strength at control point i
ρ	fluid density

I.   Introduction

Interest in man-portable small unmanned air vehicles (SUAVs) has heightened recently as miniaturized autopilot and sensor capabilities have improved and increasingly complex SUAV missions have been conceived. Typical fixed wing SUAV configurations are often limited in their practical application due to the requirement of large take-off and landing areas and/or specialized take-off and landing equipment. In addition, the capability to persistently sense an area via a "perch-and-stare" approach has long been desired. In this mission scenario, the SUAV would be required to fly to a remote location, land, collect sensor data for an extended period of time, then takeoff and return to a specified rendezvous point—all without human assistance. These drawbacks and desired capabilities, among others, have directed attention toward the development of vertical take-off and landing (VTOL) SUAVs, specifically tail-sitter designs.

The concept of a tail-sitter VTOL aircraft has been around for over half a century. The main attraction of such an aircraft is the ability to take off and land in a manner similar to a rotorcraft, yet transition to efficient horizontal flight, thus achieving higher flight speeds and longer endurance and range. Likely, the most famous of these aircraft are the Convair XFY-1 Pogo (see Fig. 1) and the Lockheed XFV-1, developed and tested in the 1950's. These planes quickly proved that the tail-sitter concept was substantially flawed, though, at least for piloted aircraft. After a relatively short test period, this concept was all but abandoned, mainly due to difficulties associated with a piloted landing (one must realize that the pilot was essentially laying on his back with no real view of the ground while trying to descend onto a target). However, when dealing with unmanned air vehicles under automatic control, this problem no longer exists, and the tail-sitter becomes (at least conceptually) a viable solution.

Figure 1. The Convair XFY-1 Pogo in hovering flight.

The development of such VTOL aircraft presents many challenges for SUAVs, including power, controls, and aerodynamic modeling. VTOL aircraft experience airflow situations very foreign to conventional aircraft. For example, propwash effects are of secondary importance and are often ignored in preliminary designs of conventional aircraft, but cannot be neglected in the development of VTOL aircraft. Specifically during take-off, hovering, and landing, propwash effects become dominant because freestream flow from the aircraft's forward velocity is almost negligible. Additionally, current design tools are almost exclusively based on purely inviscid flow assumptions, which are questionable for Reynolds numbers less than 800,000, and certainly inadequate for Reynolds numbers less than 200,000. Thus, it becomes necessary to address, at least at some level, viscous effects in the early development of any SUAV aircraft.

Commonly, computational fluid dynamics (CFD) and/or experimental trial and error are used as "design tools" for development of fixed-wing SUAVs. Although one cannot argue that some success has been achieved, the time required to obtain results from these methods is too great to efficiently be used during the initial design phase. Rather, these are viable analysis tools to be employed after a design has reached some level of maturity. A design tool, then, that rapidly and correctly predicts geometry, propwash, and Reynolds number effects on aerodynamic forces and moments is desirable. This paper presents a candidate approach based on a numerical lifting line algorithm for the wing aerodynamics. The method presented here extends the original algorithm to allow viscous effects on the 2D section lift and drag behavior, and the effects of non-uniform airflow over a wing (i.e. propwash effects). This approach, rooted in inviscid theory, accounts for the effects of viscosity on the lift, drag, and moment behavior via semi-empirical corrections to an otherwise potential flow solution. For the propeller aerodynamics, a combination of blade element theory coupled with momentum equations is employed. The resulting flowfield is added to the freestream velocity to create the input flowfield for the with aerodynamic model.

II.   Lifting Line Formulation

A.   Overview

In the numerical lifting line method presented by Phillips,[1] a finite wing is modeled using a series of horseshoe vortices with one edge bound to the quarter chord of the wing and the trailing portion aligned with the freestream velocity. A general 3D vortex lifting law is combined with Prandtl's hypothesis that each spanwise section of the wing has a section lift equivalent to that acting on a similar 2D airfoil with the same local angle of attack.

From the 3D vortex lifting law, the differential force vector produced by the finite wing section i is

$$\mathbf{dF_i} = \rho \Gamma_i \mathbf{V_i} \times \mathbf{d\ell_i} \tag{1}$$

The lift coefficient of a 2D airfoil can be expressed as an arbitrary function of angle of attack and flap deflection

$$C_{L_i} = C_{L_i}(\alpha_i, \delta_i) \tag{2}$$

Assuming that this relationship is known at each section, the magnitude of the differential force produced by wing section i is

$$dF_i = \frac{1}{2}\rho V_i^2 C_{L_i}(\alpha_i, \delta_i) A_i \tag{3}$$

Setting the magnitude of Eq. (1) equal to the right hand side of Eq. (3) for each of the spanwise sections of the wing produces a system of equations that can be solved for the vortex strengths at each section. Once all the vortex strengths are known, the force vector at each section can be computed and summed together to determine the force and moment vectors acting on the wing. This method has been shown to work well at predicting the inviscid forces and moments for wings with sweep and dihedral and aspect ratios greater than four. Accuracy is similar to panel methods or Euler computational fluid dynamics, but at a fraction of the cost. In addition, systems of lifting surfaces with arbitrary position and orientation can be analyzed.

B.   Vortex Strengths

Typically, the numerical lifting line algorithm is developed in a nondimensional form. This is appropriate for conventional aircraft where the freestream velocity is used as a parameter for nondimensionalization.

However, for VTOL flight analysis, where the freestream velocity can approach zero, a dimensional approach is better suited.

We begin by setting the magnitude of the force obtained from the section lift coefficient at wing section i, Eq. (3) equal to the magnitude of the forces determined from the 3D vortex lifting law, Eq. (1). After some rearrangement, we obtain

$$2\left|\Gamma_i\left(\mathbf{V_{rel_i}} + \sum_{j=1}^{N}\Gamma_j\mathbf{v_{ji}}\right)\times d\boldsymbol{\ell_i}\right| - V_{tot_i}^2 A_i C_{Li}(\alpha_i, \delta_i) = 0 \tag{4}$$

Note that on the LHS, the velocity of section i is split into the local upstream velocity $\mathbf{V_{rel_i}}$ and the velocity induced by all horseshoe vortices in the system (initially of unknown strength). The local upstream velocity differs from the global freestream velocity in that it may also have contributions from prop-wash or rotations of the lifting surface about the aircraft center of gravity. The magnitude of the total velocity at wing section i is denoted as

$$V_{tot_i} = |\mathbf{V_{tot_i}}| = \left|\left(\mathbf{V_{rel_i}} + \sum_{j=1}^{N}\Gamma_j\mathbf{v_{ji}}\right)\right| \tag{5}$$

In the above expressions, $\mathbf{v_{ji}}$ is the normalized velocity induced at section i by horseshoe vortex j, calculated as

$$\mathbf{v_{ij}} = \frac{1}{4\pi}\left[\delta_{ij}\frac{(r_{i_1j} + r_{i_2j})(\mathbf{r_{i_1j}}\times\mathbf{r_{i_2j}})}{(r_{i_1j}r_{i_2j}(r_{i_1j}r_{i_2j} + \mathbf{r_{i_1j}}\cdot\mathbf{r_{i_2j}})} + \frac{\mathbf{u_\infty}\times\mathbf{r_{i_2j}}}{r_{i_2j}(r_{i_2j} - \mathbf{u_\infty}\cdot\mathbf{r_{i_2j}})} - \frac{\mathbf{u_\infty}\times\mathbf{r_{i_1j}}}{r_{i_1j}(r_{i_1j} - \mathbf{u_\infty}\cdot\mathbf{r_{i_1j}})}\right] \tag{6}$$

where δ_{ij} is the Kronecker delta (1 if $i = j$, 0 if $i \neq j$). Equation (4) defines a system of equations that can be solved for the unknown horseshoe vortex strengths Γ_i. The system is nonlinear and can be written in the vector form

$$f(\mathbf{\Gamma}) = \mathbf{R} \tag{7}$$

where

$$f_i(\mathbf{\Gamma}) = 2\left|\Gamma_i\left(\mathbf{V_{rel_i}} + \sum_{j=1}^{N}\Gamma_j\mathbf{v_{ji}}\right)\times d\boldsymbol{\ell_i}\right| - V_{tot_i}^2 A_i C_{Li}(\alpha_i, \delta_i) \tag{8}$$

We seek the vector of horseshoe vortex strengths $\mathbf{\Gamma}$ that forces the residual vector $\mathbf{R}$ to zero. This is accomplished using simple Newton iterations. Starting with an initial guess for $\mathbf{\Gamma}$, we can compute the iterative change from

$$[\mathbf{J}]\mathbf{\Delta\Gamma} = -\mathbf{R} \tag{9}$$

where $[\mathbf{J}]$ is the N by N Jacobian matrix:

$$J_{ij} = \frac{\partial f_i}{\partial \Gamma_j} \tag{10}$$

This $\mathbf{\Delta\Gamma}$ is applied to the previous estimate of $\mathbf{\Gamma}$ and iterations are continued until convergence criterion are met.

Evaluating the partial derivatives of Eq. (8), we obtain

$$J_{ij} = \delta_{ij}2|\mathbf{W_i}| + \frac{2\mathbf{W_i}\cdot(\mathbf{v_{ji}}\times d\boldsymbol{\ell_i})}{|\mathbf{W_i}|}\Gamma_i$$
$$- V_{tot_i}^2 A_i \frac{\partial C_{Li}}{\partial \alpha_i}\frac{V_{ai}(\mathbf{v_{ji}}\cdot\mathbf{u_{ni}}) - V_{ni}(\mathbf{v_{ji}}\cdot\mathbf{u_{ai}})}{V_{ai}^2 + V_{ni}^2} - 2A_i C_{Li}(\alpha_i, \delta_i)(\mathbf{V_{tot}}\cdot\mathbf{v_{ji}}) \tag{11}$$

where again, δ_{ij} is the Kronecker delta, and

$$\mathbf{W_i} = \left(\mathbf{V_{rel_i}} + \sum_{j=1}^{N}\Gamma_j\mathbf{v_{ji}}\right)\times d\boldsymbol{\ell_i} \tag{12}$$

In Eq. (11) V_{ai} and V_{ni} are the axial and normal components of the local velocity, respectively:

$$V_{ai} = \left(\mathbf{V_{rel_i}} + \sum_{j=1}^{N} \Gamma_j \mathbf{v_{ji}} \right) \cdot \mathbf{u_{ai}} \tag{13}$$

$$V_{ni} = \left(\mathbf{V_{rel_i}} + \sum_{j=1}^{N} \Gamma_j \mathbf{v_{ji}} \right) \cdot \mathbf{u_{ni}} \tag{14}$$

where $\mathbf{u_{ai}}$ is the unit vector in the axial (chordwise) direction of section i, and $\mathbf{u_{ni}}$ is the unit vector in the normal direction of section i. It should be noted that when airfoil sections experience angles of attack beyond stall, the zero slope of the C_L vs. α curve causes divergence of the Newton iterations. In this case, a simple under-relaxed Picard iteration procedure is used to solve for the Γ_is.

In order to achieve the convergence criteria with a small number of iterations, it is important to obtain a good initial guess for $\mathbf{\Gamma}$. To do this, Phillips[1] suggests finding first a linearized approximation. This system is constructed from the original system of equations, Eq. (8), by dropping all second order terms and using the small angle approximation for the geometric and induced angles of attack. This results in the linear system

$$\frac{2}{A_i C_{L\alpha i}} |\Gamma_i (\mathbf{V_{rel_i}} \times \mathbf{d\ell_i})| - V_{rel_i}^2 \left(\sum_{j=1}^{N} \Gamma_j \mathbf{v_{ji}} \cdot \mathbf{u_{ni}} \right) = V_{rel_i}^2 (\mathbf{V_{rel_i}} \cdot \mathbf{u_{ni}} - \alpha_{L0i} + \epsilon_i \delta_i) \tag{15}$$

Once this system is solved for the Γ_is, they are used as the initial guess for the Newton iterations.

C. Aerodynamic Forces and Moments

Once the magnitude of Γ_i at each wing section has been found, the forces resulting from the vortex strengths can be summed to find the overall force and moment acting on the aircraft. The total force on the aircraft is found by summing Eq. (1) over all wing sections:

$$\mathbf{F} = \rho \sum_{i=1}^{N} \left[\Gamma_i \left(\mathbf{V_{rel_i}} + \sum_{j=1}^{N} \Gamma_j \mathbf{v_{ji}} \right) \times \mathbf{d\ell_i} \right] \tag{16}$$

Equation (16) provides the total inviscid force vector acting on the aircraft, and can be divided into the typical lift and induced drag components. A correction for the viscous drag[2] is added to the model based on the 2D airfoil drag behavior as a function of angle of attack:

$$\delta\mathbf{F}_{visc} = \sum_{i=1}^{N} \frac{1}{2} \rho V_{tot_i}^2 \bar{c}_i C_{Di} \mathbf{u_i} \tag{17}$$

where C_{D_i} is the local 2D section drag coefficient (evaluated at the local angle of attack).

Similarly, the overall moment vector acting on the aircraft can be found from

$$\mathbf{M} = \rho \sum_{i=1}^{N} \mathbf{r_i} \times \left[\Gamma_i \left(\mathbf{V_{rel_i}} + \sum_{j=1}^{N} \Gamma_j \mathbf{v_{ji}} \right) \times \mathbf{d\ell_i} \right] + \delta\mathbf{M_i} \tag{18}$$

where the first term is the moment due to the aerodynamic forces at each section acting at a moment arm about the center of gravity, and the second term $\delta\mathbf{M_i}$ is the 2D quarter-chord moment generated by each spanwise segment. $\delta\mathbf{M_i}$ can be easily obtained if we assume a constant moment coefficient over each wing section:

$$\delta\mathbf{M_i} = -\frac{1}{2} \rho \mathbf{V_{tot_i}}^2 C_{Mi} \int_{s0}^{s1} c^2 \, ds \, \mathbf{u_{si}} \tag{19}$$

where $\mathbf{u_{si}}$ is the unit vector in the spanwise direction.

A viscous correction[2] is also added to the overall moment vector to take into account the additional moment caused by the viscous drag force at each spanwise wing section:

$$\delta\mathbf{M}_{visc_i} = \sum_{i=1}^{N} \frac{1}{2} \rho V_{tot_i}^2 S_i C_{Di} (\mathbf{r_i} \times \mathbf{u_i}) \tag{20}$$

III.   Propeller Model Formulation

In order to predict the time-averaged slipstream behind a propeller, an induced velocity must be calculated immediately behind the propeller. This velocity is a function of radius if the propeller axis is in line with the freestream velocity vector, and a function of radius and azimuthal angle, θ, if the propeller is not aligned with the freestream. Phillips[2] presents an approach that does not constrain the freestream velocity to be aligned with the propeller axis. Thus, off-axis moments and forces from the propeller can be found. Dividing the propeller into N discrete intervals, the induced velocity at each radial blade element can be found by relating the section circulation to the section induced tangential velocity as shown in Eq. (21).

$$b\Gamma = 4\pi\kappa r V_{\theta i} \tag{21}$$

Substituting Prandtl's tip loss factor[3] for Goldstein's κ factor, the following equation is produced:

$$\frac{bc_b}{16r}C_l - \cos^{-1}\left(exp\left[-\frac{b\left(1 - \frac{2r}{D_p}\right)}{2\sin\beta_t}\right]\right)\tan\epsilon_i\sin(\epsilon_\infty + \epsilon_i) = 0 \tag{22}$$

which can be numerically solved for ϵ_i. Once ϵ_i is known for a given blade section, the total induced velocity is found from

$$V_i = \frac{\omega r \sin\epsilon_i}{\cos\epsilon_\infty} \tag{23}$$

This velocity vector is then divided into its axial and tangential components.

Once the induced axial and tangential velocities are known at the propeller plane, the flowfield behind the propeller can be estimated by applying momentum equations. The slipstream radius at a distance s behind the propeller is found by solving for the slipstream development factor suggested by McCormick:[4]

$$B_d = 1 + \frac{s}{\sqrt{s^2 + R_d^2}} \tag{24}$$

where B_d is the development factor and approaches 2 as the distance from the propeller plane (s) approaches infinity. Using this radius, and applying conservation of mass and angular momentum as suggested by Stone,[5] the development of the axial and tangential velocities throughout the slipstream are found.

A.   Model Assumptions

This approach to modeling the propeller flowfield implies several underlying assumptions, which are discussed below.

- The propeller aerodynamics affect the wing, but the wing aerodynamics do not affect the propeller. This allows for the combined wing and propeller models to first solve the propeller behavior and then solve for the aerodynamics of the wing in the resultant flowfield. No iterations need be performed between the flowfields of the wing and propeller, which provides for a faster solution.

- The axis of the propeller slipstream stays coincident with the axis of the propeller. This can be assumed if the forward velocity of the aircraft is always much greater than the sideslip velocity.

- There is no mixing between the slipstream and the freestream velocities. No adjustments are made at the edges of the slipstream to account for mixing with the freestream. This is obviously a significant assumption, but accounting for these effects is beyond the scope of this initial-stage aerodynamic model.

- Finally, the resultant induced velocities at any distance behind the propeller (s) are assumed constant with varying azimuthal angle. Therefore, although the induced velocity downstream from the propeller is a function of θ when the propeller is at an angle of attack, the *average* velocity at that radius and distance from the propeller is taken as the induced velocity.

IV.   Results

A.   Irrotational Slipstream

As a first check on the numerical lifting line algorithm, inviscid estimates of wing lift and induced drag coefficient for straight and swept wings in a uniform freestream were computed. The section lift coefficient was defined as a linear function of angle of attack, and the section parasite drag was set to zero. For this case, this algorithm exactly reproduces the results of the original numerical lifting line algorithm.[1]

To determine the ability of this method to predict the effects of the propeller slipstream, results are compared to the experimental data of Stuper.[6] In these experiments, conducted in the 1930's, the aerodynamics of a finite wing were investigated in the presence of a slipstream. A Göttingen 409 airfoil section was employed on a rectangular wing of aspect ratio four (0.8 m span, 0.2 m chord) with circular end caps of diameter 0.32 m. Precautions were taken in the experimental setup to ensure that the slipstream produced by the 0.12 m diameter jet was both uniform and non-rotational. The freestream velocity was nominally 30 m/s, with jet speeds of 35.4 m/s and 40.8 m/s, representing 18% and 36% velocity increases in the slipstream, respectively.

For the numerical model, the 2D section lift behavior as a function of angle of attack is required. This behavior can be obtained either numerically or experimentally. Experimental results for the Göttingen 409 airfoil were not readily found in the literature, so instead a 2D incompressible Reynolds-Averaged Navier-Stokes (RANS) solution was used. For this, a pressure-based, segregated finite-volume solver was employed. In terms of the solution/discretization procedure, the convective terms were computed using a second-order upwind discretization, while the viscous terms were discretized using a second-order central discretization. Pressures were interpolated to the cell faces using a second-order interpolation scheme, and pressure-velocity coupling was achieved using the common SIMPLEC algorithm. Figure 2 shows the grid-converged results at Re= $406,000$ using the Spalart-Allmaras[7] turbulence model. Although it is not expected that this model predicts the behavior beyond stall with a large degree of accuracy, it provides sufficiently accurate behavior in the absence of experimental data.
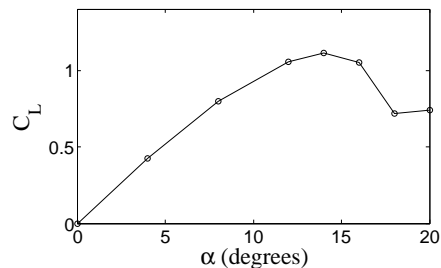

Figure 2. C_L **vs.** α **for the Göttingen 409 airfoil at Re**$= 406,000$ **as predicted by the RANS equations.**

The end caps employed in Stuper's experiments significantly effect the lift behavior of the wing. To numerically model these circular caps, vertical rectangular wing sections were included at the wing tips. Great care was taken to ensure that the effects of these rectangular surfaces correctly represented the effects of the circular caps. The dimensions of the caps were altered until the lift distribution near the wing tips agreed with the experimental data for the case of uniform flow. Figure 3 illustrates the numerical geometry, showing the wing and representative size of the slipstream. Note that the chord-wise lines represent the distribution of the 2D spanwise wing sections.
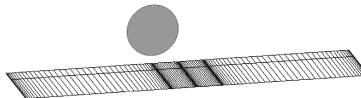

Figure 3.   Computer model of the finite wing geometry showing the distribution of the spanwise sections. The circular disk illustrates the size of the jet relative to the wing.

Figure 4 shows a comparison of the resulting numerical solutions with the experimental C_L distributions at three angles of attack. The similarity in behavior near the tips indicates that the rectangular surfaces model well the circular end caps used in the experiments. Note that the C_L distribution across the entire
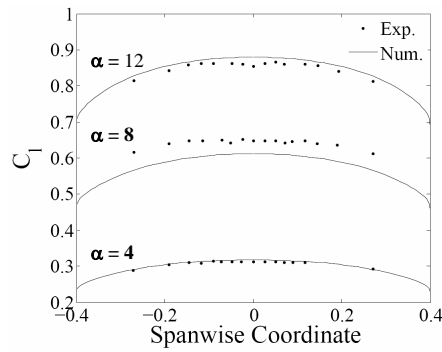
Figure 4. C_L distribution across the wing at three angles of attack with a uniform freestream velocity. Experimental values are from Stuper.[6]

wing at both 4° and 12° angle of attack agree very well. At $\alpha = 8°$, however, the magnitude of the lift forces are under-predicted. This discrepancy is a result of a "jump" in the experimentally measured lift that occurs near $\alpha = 8°$. This "jump," seen in Fig. 7 is not predicted by the 2D RANS solution used as an input into the lifting line algorithm.

The experimentally measured upstream velocity profiles were used as inputs to the numerical model, and are shown in Fig. 5. These profiles are altered slightly from the experiments in that they represent symmetrically "averaged" profiles (the measured profiles exhibit some asymmetric behavior that is ignored in the numerical model). Note that a significant velocity deficit occurs near the edge of the slipstream. Stuper attributes this deficit to viscous effects on the jet nozzle placed upstream of the wing.
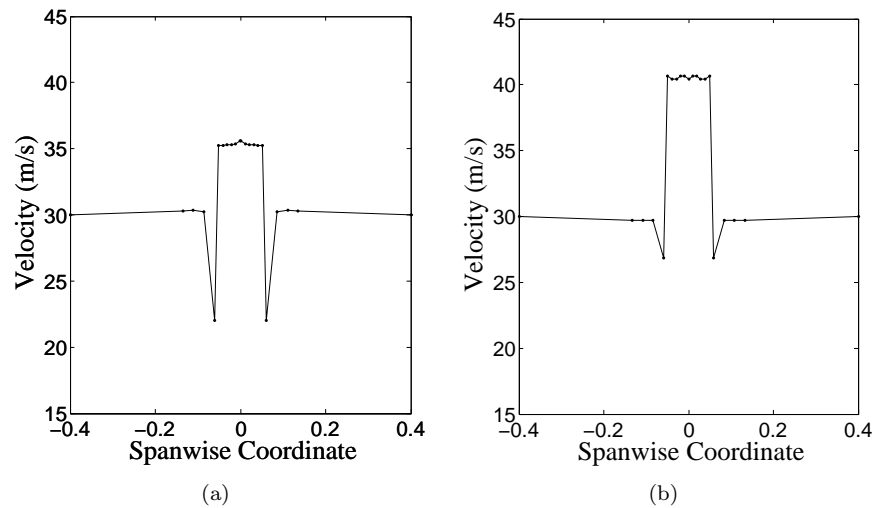

(a)

(b)

Figure 5. Upstream velocity profiles for (a) 18% and (b) 36% increase in freestream velocity in the slipstream, as based on the measurements of Stuper.[6]

Using the (nonlinear) airfoil section lift behavior obtained from the RANS equations, the upstream velocity profiles obtained from the published experiments, and the geometry shown in Fig. 3, results were obtained at three different angles of attack for both the 18% and 36% jets. The numerical solution required 19 Newton iterations to converge—about six seconds of CPU time on a Pentium 4 PC—for the worst case (36% jet at $\alpha = 8°$). The resulting lift distributions are shown in Fig. 6 along with the experimental values.

The numerical analysis shows good agreement with the experimental data. At both $\alpha = 4$ and 12 degrees the numerical results inside the jet profile lie within the uncertainty of the experimental data. However, note that the numerical results at $\alpha = 8$ are slightly lower than the experimental values. This is again accounted for by the jump in the experimental C_L value at $\alpha = 8$ that was not predicted by the 2D RANS calculations. Additionally, there are small dips in the distribution C_L near the edges of the slipstream that do not appear in the computer model. It was found, however, that such dips could be attained in the computer model
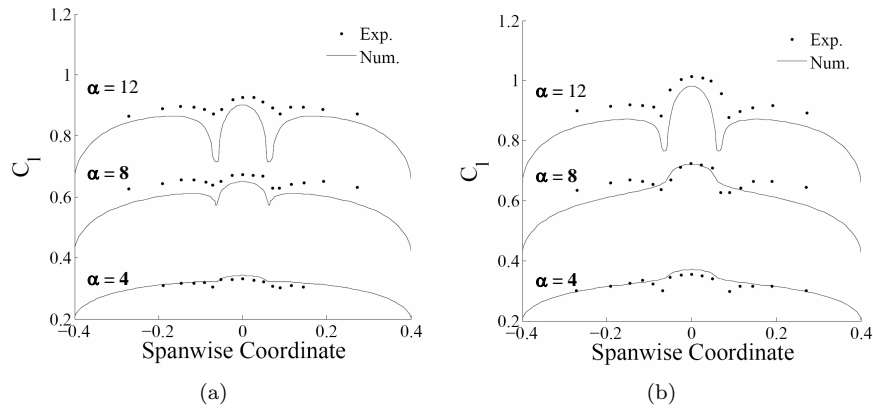
Figure 6. C_L distribution along the span for slipstream velocity (a) 18% and (b) 36% at three angles of attack. Experimental values are from Stuper.[6]

by slightly altering the upstream velocity profiles such that the velocity at the edge of the jet dropped approximately 3 m/s lower than the profiles assert in Fig. 5. With only a single experimental measurement in the velocity "dip" it is unclear whether or not the minimum velocities shown in Fig. 5 are actually the minimum velocities in the flow. Therefore, if more accurate velocity profiles were given, it is possible that the analytical results would better predict the experimental lift distribution results. Further, at both 8° and 12° angle of attack, the experimental C_L values outside of the slipstream are noticeably higher than the numerical results.

Also of interest is the overall C_L vs. α behavior for the finite wing with and without the slipstream. Figure 7 shows the experimental and numerical results for the coefficient of lift over a range of angles of attack. Note that the numerical model matches the data very well at angles of attack below stall. The numerical analysis predicts an increase in overall lift with increasing jet velocity which agrees with the experimental data. The jump in the experimental C_L measurements at $\alpha = 8$ degrees is seen here. As stated previously, this jump was not found in the 2D RANS results.
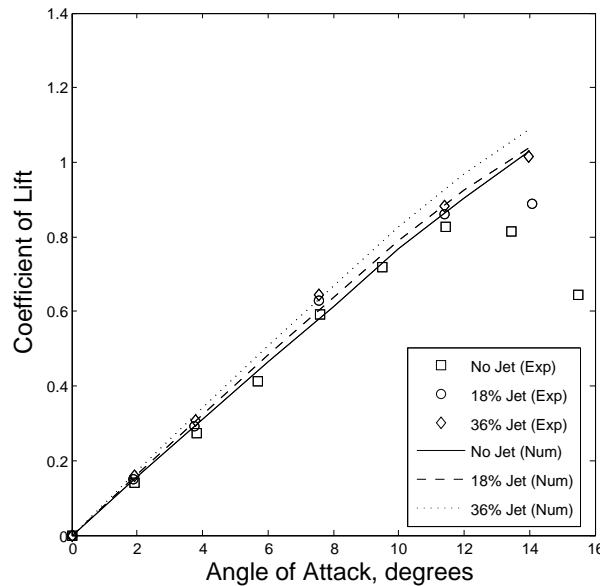

Figure 7. Overall C_L vs. α for the finite wing. Experimental values are from Stuper.[6]

B. Rotational Slipstream

In this section, the propeller and wing aerodynamic models are coupled. First, however, the performance of the propeller model alone is presented. Figure 8 shows the numerical results vs. time averaged experimental data taken by Lepicovsky[8] immediately behind the propeller. Only basic parameters of the experimental propeller are included in the literature, so two assumptions were made: 1) the chord has an elliptical distribution along the span of the propeller blade, 2) the airfoil has lift and drag characteristics of a NACA 0012. The results show excellent agreement, although the lack of slipstream interaction with the freestream is apparent in the numerical model.
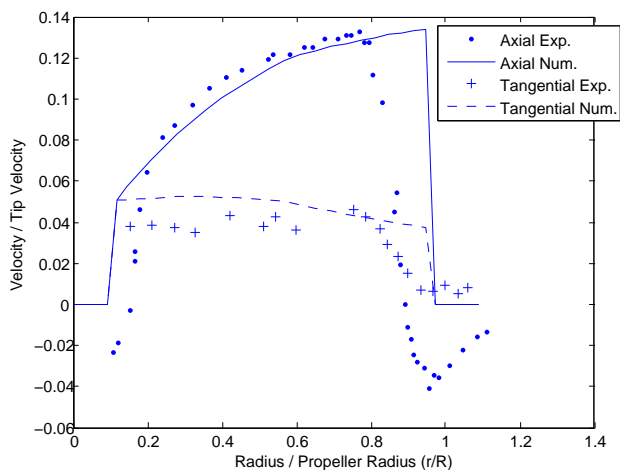

Figure 8. Normalized time-averaged velocities behind the propeller vs. normalized propeller radius. Experimental values are from Lepicosvsky.[8]

Behavior of the model further down in the slipstream is seen in Fig. 9. Figure 9a displays the numerical model predictions of the slipstream radius (white line) overlaid on the experimental data taken by Nozicka.[9] The data was taken at an advance ratio of 0 and highlights the strong slipstream contraction at static thrust conditions. Figure 9b displays the numerical model velocity field behind the propeller. The color coding of each of the two figures are identical, and referenced according to the color scale at the right of the figure. From these contour plots it can be noted that the velocity magnitudes within the slipstream of the numerical solution match experimental data quite well. The slipstream radius of the numerical model appears to become more accurate to the experimental data as it moves further downstream. Other cases were tested at various advance ratios with similar results.
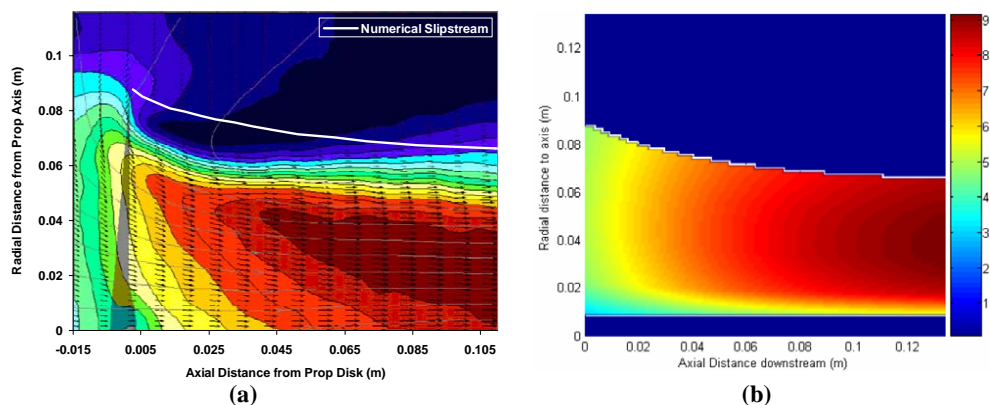

Figure 9. (a) Experimental axial velocity flowfield of a propeller at $J = 0$ as measured by Nozicka,[9] overlaid with the numerical prediction of the slipstream edge. (b) Numerical prediction of the flowfield of a propeller at $J = 0$. The color bar at the right has units of (m/s) and is applicable to both figures.

Finally, the numerical propeller and wing aerodynamic models are integrated into a single model to

simulate the effects of propwash on the lift distribution along a finite wing. The same wing geometry used by Stuper[6] presented in the previous section is employed here. The propeller used in the experiments and numerics has a diameter of 15cm and a pitch of 6cm. The propeller was placed in the model 12.5cm in front of the wing quarter chord and rotated at an advance ratio of 0.15 in the 30m/s freestream. Figure 10 shows the resulting prediction for the C_l distribution across the wing.
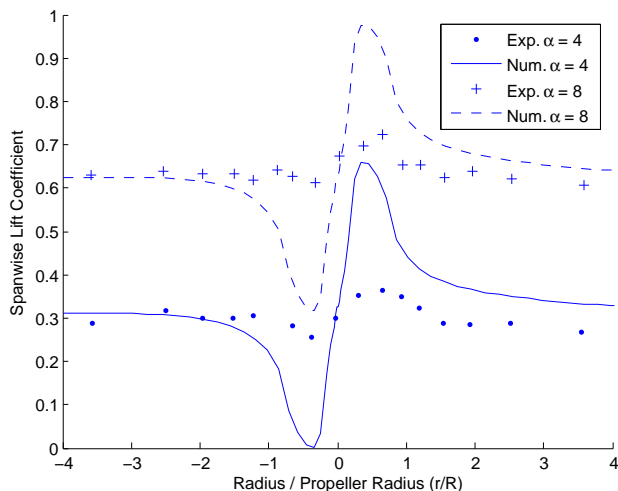

Figure 10. C_l **distribution along the span of a wing in a propeller slipstream. Experimental values are from Stuper.**[6]

Note that the numerical results are qualitatively correct, but quantitatively optimistic. It should be noted that only standard pitch and diameter values are presented for the propeller used in the experiments. It is likely that a more accurate representation of the actual propeller will result in better agreement with the experimental data (although it is not expected to completely resolve the discrepancies in magnitude seen in the figure). The numerical lifting-line approach implemented in the wing aerodynamic model is also likely over-predicting the lift across the wing. Further investigation into the results of this scenario, as well as investigations using the experimental data from Robinson[10] and Brenckmann[11] are underway.

V.   Conclusions and Future Work

The results of the low-cost model presented above indicate that this approach shows promise for initial aerodynamic design calculations of wings with significant slipstream effects. The lifting line approach to modeling the wing aerodynamics produces satisfactory results in the presence of a slipstream, often to within the uncertainty of the experimental measurements. The propeller model also produces results in good agreement with experimental data. However, the combined wing and propeller models produce results that, although qualitatively correct, tend to over-predict the magnitude of the lift perturbations due to the slipstream. This behavior and its possible remedies are currently under investigation.

References

[1]Phillips, W. F. and Snyder, D. O., "Modern Adaptation of Prandtl's Classic Lifting-Line Theory," *Journal of Aircraft*, Vol. 37, 2000, pp. 662–670.

[2]Phillips, W. F., *Mechanics of Flight*, John Wiley & Sons Inc., Hoboken, New Jersey, 2004.

[3]Prandtl, L. and Betz, A., *Vier Abhandlungen zur Hydrodynamik und Aerodynamik*, Gottingen, 1927.

[4]McCormick, B. W., *Aerodynamics, Aeronautics, and Flight Mechanics*, John Wiley & Sons Inc., New York, 1979.

[5]Stone, R. H., "Aerodynamic Modelling of a Wing-in-Slipstream Tail-Sitter UAV," *AIAA 2002 Biennial International Powered Lift Conference and Exhibit*, 2002.

[6]Stuper, J., "Effect of Propeller Slipstream on Wing and Tail," *NACA TM 874*, 1938.

[7]Spalart, P. and Allmaras, S., "A One-Equation Turbulence Model for Aerodynamic Flows," *AIAA Paper 92-0439*, 1992.

[8]J. Lepicovsky, W. B., "Aerodynamic Measurements About a Rotating Propeller with a Laser Velocimeter," *Journal of Aircraft*, Vol. 21, 1984, pp. 264–271.

[9]J. Noika, J. N. and Matcha, J., "Research on the Flow past an Aircraft Propeller," *Proceedings of PSFVIP-4*, 2003.

[10]Robinson, R. G. and William H. Herrnstein, J., "Wing-Nacelle-Propeller Interference for Wings of Various Spans Force and Pressure-Distributuion Tests," *NACA Report No. 569*, 1936.

[11]Brenckmann, M. E., "Experimental Investigation of the Aerodynamics of a Wing in a Slipstream," *Journal of the Aeronautical Sciences*, 1958.